RESEARCH ARTICLE

Application of Artificial Potential Field Method in Three-Dimensional Path Planning for UAV Considering 5G Communication

YESHUANG TANG[ID], HAOXIAN CHEN[ID], ZHAOYONG MA, ZICHEN JIN[ID], AND HUILI YIN[ID]

College of Electronic Engineering (College of Artificial Intelligence), South China Agricultural University, Guangzhou 510000, China

Corresponding author: Huili Yin (huiliyin@scau.edu.cn)

ABSTRACT Maintaining robust communication between UAV(Unmanned aerial vehicle) and host computers is pivotal for ensuring the security and reliability of UAV in executing automated tasks. The advent of 5G, the latest generation of mobile communication technology, presents an opportunity to establish low-latency and high-reliability communication links between UAV and host computers. While automatic flight schemes of UAV are typically calculated through three-dimensional path planning, existing schemes often overlook the communication quality between UAV and the host computer during flight execution. This study proposes a novel approach to three-dimensional path planning that integrates considerations of 5G communication intensity into the traditional artificial potential field (APF) method. Utilizing ray tracing method, the average 5G communication intensity within a given region is computed, and areas with optimal average 5G communication quality are identified as 5G secondary gravitational points. These points guide the UAV's three-dimensional path toward regions with superior 5G communication quality. To address the challenge of local minimum traps inherent in traditional APF methods, this study proposes employing a fuzzy control algorithm to generate auxiliary forces, enabling UAV to avoid such traps proactively. Simulation experiments conducted using MatlabR2023b validate the efficacy of the proposed approach. Results demonstrate that the enhanced APF method effectively mitigates local minimum problems, albeit with a marginal increase in average path length (13.7769%). Notably, the average path's 5G communication intensity experiences a substantial improvement (20.7919%), indicating that the algorithm prioritizes enhancing communication quality at the expense of slightly longer paths. Moreover, in scenarios with severe signal masking at the transmitter, the algorithm exhibits even greater improvements in average path 5G communication intensity.

INDEX TERMS 5G, artificial potential field, three-dimensional path planning, ray tracing, fuzzy control.

I. INTRODUCTION

The aerial unmanned aerial vehicle (UAV), comprises a fundamental system consisting of the UAV itself, a host computer, and communication equipment facilitating communication between the UAV and the host computer. Over recent years, propelled by rapid advancements in the UAV industry, the applications of UAV has diversified extensively. From rudimentary transportation tasks, UAV has expanded

The associate editor coordinating the review of this manuscript and approving it for publication was Emrecan Demirors[ID].

their scope to encompass a myriad of complex missions, including high-altitude inspection, agricultural and forestry operations, geographic mapping, urban aerial photography, and detection and rescue missions. To execute these multifaceted tasks efficiently, UAV necessitates high-precision automatic control, entailing the development of automated, efficient, and safe flight plans. The advent of the latest cellular mobile communication network technology, 5G, has changed UAV operations by enabling real-time transmission of ultra-high-definition imagery and remote low-latency control between UAV and host computers. However, it's

crucial to note that communication in the 5G millimeter wave band primarily relies on line-of-sight (LOS) communication. LOS obstacles, such as people, buildings, and structures, pose a significant challenge as they attenuate signals, thereby compromising communication quality. Regrettably, most existing UAV three-dimensional path planning algorithms focus solely on route length and safe obstacle avoidance, neglecting the crucial factor of communication intensity. Consequently, communication blockages may occur during flight, posing security risks to the UAV's automated flight plans. Addressing this issue necessitates a holistic approach to path planning that incorporates considerations of communication intensity to ensure uninterrupted communication and enhance the overall safety and efficiency of UAV operations.

Path planning plays a critical role in defining the flight trajectory of UAV. Among the commonly used three-dimensional path planning algorithms are the Dijkstra algorithm [1], A* algorithm [2], genetic algorithm (GA) [3], particle swarm optimization (PSO) [4], ant colony algorithm (ACO) [5], and artificial potential field (APF) [6]. APF, owing to its simple principles and high computational efficiency, is extensively employed in UAV three-dimensional path planning. Despite not always generating the shortest path, the APF algorithm excels in producing relatively smooth flight paths for UAV, facilitating safer obstacle avoidance with smoother trajectories. The fundamental principle of APF involves simulating UAV movement within a virtual potential field composed of gravitational and repulsive components. In this virtual field, target points exert gravitational forces on UAV, while obstacles exert repulsive forces. As a result of the total force, UAV navigates towards target points while circumventing obstacles. However, APF suffers from a notable drawback: the potential for falling into local minimum traps, where gravitational and repulsive forces cancel each other, rendering UAV unable to progress. To address this limitation, numerous solutions have been proposed by researchers. In [7], virtual obstacles are strategically placed near local minima points to steer UAV away. Reference [8] proposes the simulated annealing algorithm to escape local minima, while [9] combines the Bug algorithm with wall-following techniques for the same purpose. Additionally, [10] suggests establishing temporary local target points to guide UAV away from local minima, thereby ensuring continued progress along the planned trajectory.

The accuracy of the 5G channel model significantly impacts the performance of wireless communication systems, which, in turn, affects the communication quality between UAV and host computers during flight operations. Previous research efforts have extensively explored 5G millimeter wave channel modeling, categorizing methods into three main types: Stochastic Model, Semi-Deterministic Channel Model, and Deterministic Channel Model. The Stochastic Model achieves channel modeling by extracting statistical characteristics from channel measurement data and incorporating probability distribution models. This approach considers environmental factors and model evolution effects, yielding more accurate and effective predictions when applied in environments similar to the model. Stochastic channel models include the Geometric Stochastic Model (GBSM) [11], Non-Geometric Stochastic Model (NGSM) [12], Graph-Based Model, and Saleh-Valenzuela (SV) [13] model. GBSM encompasses Regular-Shaped and Irregular-Shaped models, while NGSM includes the Tapped Delay Line and Clustered Delay Line models. Semi-Deterministic channel modeling leverages Stochastic geometric scenes and deterministic multipath relationships to describe channel characteristics. This model requires less detailed scene parameters and typically offers higher prediction accuracy than Stochastic channel models. Semi-Deterministic channel models include Map-based [14] and Quasi-Deterministic (Q-D) [15] models. On the other hand, deterministic channel modeling utilizes electromagnetic wave propagation principles to determine signal strength in any communication scenario. By employing principles such as reflection and diffraction, the model calculates received signal strength at specific positions on a 3D map with high accuracy. This approach encompasses methods such as electromagnetic simulation, ray tracing model [16], and point cloud model.

To ensure optimal communication between the UAV and the host computer during flight operations, this study proposes a novel approach: an APF three-dimensional path planning algorithm that accounts for 5G communication intensity. The algorithm identifies areas with superior communication quality within the 3D map, designating them as 5G gravitational points within the virtual potential field. By integrating these points with APF, the UAV is steered towards regions with enhanced communication quality while navigating towards the target point. Moreover, to address the challenge of local minimum traps, this study incorporates a fuzzy control algorithm. This algorithm generates auxiliary forces to prevent the UAV from getting stuck in local minima, ensuring continuous progress along the planned trajectory.

This article is structured as follows. The second section delineates the fundamental principles and prevailing issues associated with traditional APF. In the third section, the basic principle of the ray tracing method is elaborated upon, along with its application for calculating 5G communication intensity. Moving on to the fourth section, optimization techniques for addressing target unreachable scenarios, refining the obstacle repulsion model, and mitigating local minimum problems within APF are discussed. Additionally, this section explores how to integrate considerations of 5G communication intensity into APF-based path planning. In the fifth section, the proposed methodology is outlined, with insights derived from simulation tests and accompanying simulation results provided. Finally, the sixth section offers conclusions drawn from the study's findings and outlines potential avenues for future research.

II. ARTIFICIAL POTENTIAL FIELD METHOD

In traditional APF, the three-dimensional potential field is divided into two components: the gravitational field and the repulsive field. Within this virtual artificial potential field, the target point generates a gravitational field, exerting gravitational force on the UAV, while obstacles generate a repulsive field, exerting repulsive force on the UAV. As the UAV navigates towards the target point, it is consistently influenced by gravity, with the strength of gravity increasing as the UAV moves further away from the target. Consequently, the potential energy within the gravitational potential field increases proportionally. Ideally, the target point possesses the lowest potential energy value in the entire three-dimensional space, signifying the optimal position for the UAV. Guided by a combination of gravitational and repulsive forces, the UAV navigates towards the target point. Along the trajectory to the target, the UAV autonomously circumvents obstacles due to the repulsive forces exerted by them.

The gravitational potential field generated by the target point is defined as:

$$U_{att}(X) = \frac{K_{att}}{2}\rho(X, X_d). \tag{1}$$

where $X = (x, y, z)$ is the coordinate of the UAV, $X_d = (x_d, y_d, z_d)$ is the coordinate of the target point, $\rho(X, X_d)$ is the Euclidean distance from the UAV to the target point, and K_{att} is the gravitational potential field constant.

The gravity of the UAV is the negative gradient of the gravitational potential field as follows:

$$F_{att}(X) = -\nabla U_{att}(X) = -K_{att} \cdot \rho(X, X_d) \tag{2}$$

The repulsive potential field generated by the obstacle is defined as:

$$U_{rep}(X) = \begin{cases} \frac{k_{rep}}{2}\left(\frac{1}{\rho(X, X_0)} - \frac{1}{\rho_0}\right)^2, & \rho(X, X_0) \le \rho_0 \\ 0, & \rho(X, X_0) > \rho_0 \end{cases} \tag{3}$$

where $X_0 = (x_0, y_0, z_0)$ is the coordinate of the obstacle, $\rho(X, X_0)$ is the Euclidean distance from the UAV to the obstacle, ρ_0 is the influence range of the obstacle repulsion, and k_{rep} is the repulsion potential field constant.

The repulsive force on the UAV is the negative gradient of the repulsive potential field as follows:

$$\begin{aligned} &F_{rep}(X) \\ &= -\nabla U_{rep}(X) \\ &= \begin{cases} k_{rep}\left(\frac{1}{\rho(X, X_0)} - \frac{1}{\rho_0}\right)\frac{\nabla\rho(X, X_0)}{\rho^2(X, X_0)}, & \rho(X, X_0) \le \rho_0 \\ 0, & \rho(X, X_0) > \rho_0 \end{cases} \end{aligned} \tag{4}$$

The total force of UAV is the sum of the repulsive force generated by obstacles and the gravitational force generated

by the target point as follows:

$$F(X) = F_{att}(X) + \sum_{i=1}^{m} F_{rep}(X) \tag{5}$$

There are two main problems in traditional APF, which are Abbreviations Target Unreachability Problem and local minimum problem.

A. ABBREVIATIONS TARGET UNREACHABILITY PROBLEM

When obstacles are situated close to the target point, the abbreviations target unreachability problem may arise. This issue stems from the interplay of gravitational and repulsive forces. In (1), when the UAV approaches the target point, the potential energy of the gravitational field diminishes. Conversely, (3) indicates that as the UAV nears an obstacle, the potential energy of the repulsive field escalates. Consequently, if obstacles encircle the target point, the potential energy of the repulsive field near the target may outweigh the gravitational potential energy, leading the UAV to veer towards regions with ostensibly lower potential energy rather than homing in on the target. Analyzing the forces involved, obstacles in proximity to the target exert significant repulsion on the UAV, particularly when gravitational pull is minimal. This can result in the total force veering the UAV away from the target. As the UAV maneuvers away from obstacles and approaches the target anew, the gravitational force may once again become overshadowed by repulsion, perpetuating the cycle of non-convergence towards the target.

B. LOCAL MINIMUM PROBLEM

In APF, the local minimum problem is a classic issue. It arises when the repulsive force acting on the UAV equals the gravitational force in magnitude but opposes it in direction. Under this condition, the total force experienced by the UAV becomes zero, causing it to come to a standstill. This situation commonly occurs when the UAV, obstacle, and target point align on the same axis, with the obstacle positioned between the UAV and the target. During the UAV's trajectory towards the target, there will invariably be a point where the total force becomes zero. Unless additional external forces or mechanisms are applied to propel the UAV forward, it will remain stationary.

III. RAY TRACING METHOD

The ray tracing method stands as a cornerstone in deterministic channel model, leveraging principles from geometric optics (GO) theory alongside uniform theory of diffraction (UTD) to forecast radio wave propagation across diverse environments and scenarios. Beginning with the identification of the transmitter and receiver, this method launches rays in myriad directions, computing various channel attributes for each ray, including reception power, phase, delay, and polarization.

The ray tracing method is primarily categorized into two approaches: forward ray tracing method and reverse ray

tracing method. Among these, the widely employed forward ray tracing method is SBR (Shooting and Bouncing Ray), whereas the commonly utilized reverse ray tracing method is Image RT (Image Ray Tracing). In SBR, utilized in this study to assess 5G communication intensity, the transmitter emits rays uniformly in all directions within a specified angle. These rays undergo various phenomena including direct propagation, reflection, transmission, and diffraction within the known environment. Upon intersecting with objects in the environment, the ray generates channel ray beams, predominantly exhibiting direct, reflected, transmitted, and diffracted paths. When these ray beams meet preset propagation conditions (such as reflection count, propagation distance, power levels, etc.), new propagation paths are generated. This process continues until the preset propagation conditions are no longer met, at which point the calculation of the ray's propagation path ceases [17]. Subsequently, the power received at the receiver end can be computed based on the effective ray's propagation path and the receiver's position.

The received power of each ray obtained by SBR is defined as:

$$\mathrm{P}_r = \frac{P_t G_t \lambda^2 G_r}{(4\pi d)^2} \left[\prod_j R_j\right]^2 \left[\prod_k T_k\right]^2 \left[\prod_l A_l\left(s', s\right) D_l\right]^2 \tag{6}$$

where P_t is the power of the transmitter, G_t is the antenna gain of the transmitter in the direction of the ray path, λ is the wavelength of electromagnetic wave, G_r is the antenna gain of the receiver in the direction of the ray path, d is the total length of the ray path propagation between the transmitter and the receiver, R_j is the reflection coefficient of the jth reflection of the ray, T_k is the transmission coefficient of the ray at the kth transmission, $A_l\left(s', s\right)$ is the propagation loss correction factor of the diffraction path, D_l is the diffraction coefficient of the lth diffraction of the ray.

The solution of the reflection coefficient as follows:

$$R = \begin{bmatrix} R_\perp & 0 \\ 0 & R_\parallel \end{bmatrix} \tag{7}$$

where $R_\perp$ is the vertical polarization reflection coefficient of the incident plane, and $R_\parallel$ is the parallel polarization emission coefficient of the incident plane. These coefficients are derived from Fresnel reflection and transmission equations, as well as Snell's Law [18]. The coefficients $R_\perp$ and $R_\parallel$ can be expressed in terms of the incident angle (θ_i) and the relative dielectric constant (ε_r), which as follows:

$$R_\perp = \frac{\cos(\theta_i) - \sqrt{\varepsilon_r - \sin^2(\theta_i)}}{\cos(\theta_i) + \sqrt{\varepsilon_r - \sin^2(\theta_i)}} \tag{8}$$

$$R_\parallel = \frac{\varepsilon_r \cos(\theta_i) - \sqrt{\varepsilon_r - \sin^2(\theta_i)}}{\varepsilon_r \cos(\theta_i) + \sqrt{\varepsilon_r - \sin^2(\theta_i)}} \tag{9}$$

Similarly, the transmission coefficient T, the vertical polarization transmission coefficient $T_\perp$, and the parallel polarization emission coefficient $T_\perp$ are solved as shown:

$$T = \begin{bmatrix} T_\perp & 0 \\ 0 & T_\parallel \end{bmatrix} \tag{10}$$

$$T_\perp = \frac{2\cos(\theta_i)}{\cos(\theta_i) + \sqrt{\varepsilon_r - \sin^2(\theta_i)}} \tag{11}$$

$$T_\parallel = \frac{2\sqrt{\varepsilon_r}\cos(\theta_i)}{\varepsilon_r \cos(\theta_i) + \sqrt{\varepsilon_r - \sin^2(\theta_i)}} \tag{12}$$

The diffraction coefficient is computed using the UTD. A widely utilized approach involves employing a heuristic formula, often derived by analogizing the diffraction coefficient of an ideal conductor wedge. This method is particularly well-suited for computer simulations. One of the most commonly adopted heuristic diffraction formulas, proposed by Holm [19], is frequently utilized. The diffraction coefficient (D_l) as follows:

$$D^{(l)} = \frac{-e^{-\frac{j\pi}{4}}}{2n\sqrt{2\pi k}} \cot\gamma^{(l)} F\left(2kLn^2\sin^2\gamma^{(l)}\right), l = 1, 2, 3, 4 \tag{13}$$

$$\gamma^{(1)} = \frac{[\pi - (\phi - \phi')]}{2n}, \quad \gamma^{(2)} = \frac{[\pi + (\phi - \phi')]}{2n} \tag{14}$$

$$\gamma^{(3)} = \frac{[\pi - (\phi + \phi')]}{2n}, \quad \gamma^{(4)} = \frac{[\pi + (\phi + \phi')]}{2n} \tag{15}$$

$$L = \frac{S'S}{(S' + S)} \tag{16}$$

where k is the wave number, $F(x)$ is the transition function. The specific formula as follows:

$$F(x) = 2j\sqrt{x}\exp(jx)\int_{\sqrt{x}}^{\infty}\exp\left(-j\tau^2\right)d\tau \tag{17}$$

IV. IMPROVED ARTIFICIAL POTENTIAL FIELD METHOD CONSIDERING 5G COMMUNICATION INTENSITY
A. IMPROVEMENT OF ABBREVIATIONS TARGET UNREACHABILITY PROBLEM
In Section III, it is highlighted that a fundamental issue in the traditional artificial potential field method is the abbreviations target unreachability problem, stemming from the fact that the potential field value at the target point may not necessarily be the minimum value across the entire three-dimensional space. (3) illustrates that as the UAV approaches an obstacle infinitely closely, the potential energy value of the repulsive field tends to reach ∞. To address this challenge, it becomes imperative to propose a distance correction factor [20] to the repulsion field function outlined in (3). This adjustment aims to ensure that as the UAV nears the target point, the potential energy value of the repulsion field should ideally approach zero instead of ∞. Consequently, this modification ensures that the potential energy value at the target point becomes the minimum value across the entire three-dimensional space. The enhanced repulsive field
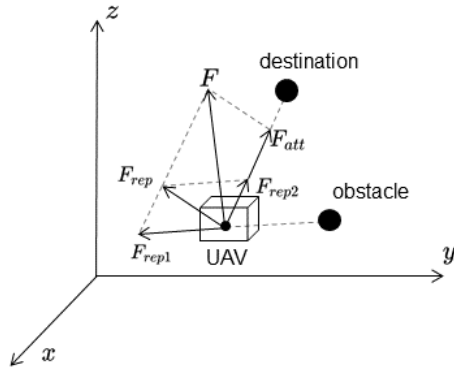
FIGURE 1. The modified force model.

function is expressed as follows:

$$
U_{rep}(X)
$$
$$
= \begin{cases} \dfrac{k_{rep}}{2}\left(\dfrac{1}{\rho(X, X_0)} - \dfrac{1}{\rho_0}\right)^2 \rho^n(X, X_d), & \rho(X, X_0) \le \rho_0 \\ 0, & \rho(X, X_0) > \rho_0 \end{cases}
$$
$$(18)$$

where $\rho^n(X, X_d)$ is the *nth* power of the Euclidean distance from the UAV to the obstacle, which is added to the repulsion field function as a distance correction factor.

The improved repulsion function as follows:

$$
\begin{aligned}
F_{rep}(X) &= -\nabla U_{rep}(X) \\
&= \begin{cases} F_{rep1}(X) + F_{rep2}(X), & \rho(X, X_0) \le \rho_0 \\ 0, & \rho(X, X_0) > \rho_0 \end{cases}
\end{aligned}
$$
$$(19)$$

where $F_{rep1}(X)$ and $F_{rep2}(X)$ are defined as:

$$
F_{rep1}(X) = k_{rep}\left(\dfrac{1}{\rho(X, X_0)} - \dfrac{1}{\rho_0}\right)\dfrac{\rho^n(X, X_d)}{\rho^2(X, X_0)} \tag{20}
$$

$$
F_{rep2}(X) = \dfrac{n}{2}k_{rep}\left(\dfrac{1}{\rho(X, X_0)} - \dfrac{1}{\rho_0}\right)^2 \rho^{n-1}(X, X_d) \tag{21}
$$

In (20) and (21), the direction of $F_{rep1}(X)$ is from the obstacle to the UAV, and the direction of $F_{rep2}(X)$ is from the UAV to the target point. The force model of UAV after the modification of the repulsion function is shown in Fig.1.

In (20) and (21), as the value of n approaches the target point where $0 < n < 1$ and UAV are in proximity, $\rho^n(X, X_d)$ tends towards zero, while $\rho^{n-1}(X, X_d)$ approaches ∞. This results in $F_{rep1}(X)$ nearing zero and $F_{rep2}(X)$ approaching ∞. Despite these converging trends, the potential energy value at the target point fails to reach its minimum.

When $n = 1$, as the UAV approaches the target point, $\rho^n(X, X_d)$ tends towards zero. Simultaneously, $F_{rep1}(X)$ approaches zero, while the magnitude of $F_{rep2}(X)$ remains constant. Despite this condition, the potential energy value at the target point fails to reach its minimum.

When $n > 1$, as the UAV approaches the target point, both $\rho^n(X, X_d)$ and $\rho^{n-1}(X, X_d)$ tend to zero. This condition

ensures that the total force acting on the UAV at the target point becomes zero, and consequently, the potential energy attains its minimum value within the entire three-dimensional space. Therefore, it is advisable to choose $n > 1$ for the value of n.

B. CALCULATION OF REPULSION FORCES FROM CYLINDRICAL OBSTACLES

In practical UAV flight scenarios, encounters with obstacles of irregular shapes are common. To streamline the computational process, this study adopts a cylindrical obstacle model for analysis. The side surface model of the cylindrical obstacle is described as follows:

$$
(x_p - x_c)^2 + (y_p - y_c)^2 = r_c^2, \quad z_p < z_c \tag{22}
$$

where (x_c, y_c, z_c) is the center coordinate of the bottom surface of the cylinder, $(x_c, y_c, 0)$ is the center coordinate of the bottom of the cylinder, (x_p, y_p, z_p) is the radius of the cylinder, (x_p, y_p, z_p) is the point on the side of the cylinder.

In traditional APF methods, the calculation of the repulsive force from obstacles typically involves computing the repulsive force exerted by a point relative to the UAV. However, since the cylindrical obstacle model employed in this study cannot be simplified to a point, an alternative approach is adopted. This study utilizes the method of computing the repulsive force from the nearest threat point to determine the repulsive force exerted by the cylindrical obstacle on the UAV [21].

The nearest threat point refers to the point X_t closest to the UAV on the side surface of the cylindrical obstacle at the same height as the UAV. The calculation of the nearest threat point X_t as follows:

$$
X_t = X_{ca} + r_c \dfrac{X - X_{ca}}{\rho(X, X_{ca})} \tag{23}
$$

where $X = (x, y, z)$ is the coordinate of the UAV, $X_t = (x_t, y_t, z_t)$ is the coordinates of the nearest threat point, $X_{ca} = (x_c, y_c, z)$ is the coordinate of the center of the cylindrical obstacle at the same height as the UAV, r_c is the radius of the cylinder, $\rho(X, X_{ca})$ is the Euclidean distance from the UAV to the center of the cylindrical obstacle at the same height as the UAV. The calculation of the most recent threat point as shown in Fig.2.

After calculating the nearest threat point, the calculation of the repulsive force generated by the cylindrical obstacle to the UAV is equivalent to the calculation of the repulsive force generated by the nearest threat point to the UAV. Finally, the calculation of the repulsive force on the UAV is modified from (19) to (24) as follows:

$$
F_{rep}(X) = \begin{cases} F_{rep1}(X) + F_{rep}(X), & \rho(X, X_t) \le \rho_0 \\ 0, & \rho(X, X_t) > \rho_0 \| z > z_c \end{cases}
$$
$$(24)$$

where $\|$ means that one of the conditions of $\rho(X, X_t) > \rho_0$ or $z > z_c$ is satisfied, ρ_0 is the influence range of obstacle
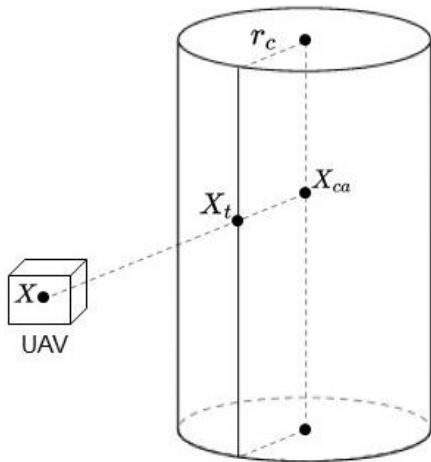
FIGURE 2. Calculation of the nearest threat point.

FIGURE 3. The schematic diagram for selecting 5G gravitational points.

repulsion, $\rho(X, X_t)$ is the Euclidean distance from the UAV to the nearest threat point, $F_{rep1}(X)$ and $F_{rep2}(X)$ are modified as follows:

$$F_{rep1}(X) = k_{\text{rep}} \left(\frac{1}{\rho(X, X_t)} - \frac{1}{\rho_0} \right) \frac{\rho^n(X, X_d)}{\rho^2(X, X_t)} \quad (25)$$

$$F_{rep2}(X) = \frac{n}{2} k_{\text{rep}} \left(\frac{1}{\rho(X, X_t)} - \frac{1}{\rho_0} \right)^2 \rho^{n-1}(X, X_d) \quad (26)$$

C. ADDRESSING THE INTENSIFICATION OF 5G COMMUNICATION

To facilitate the creation of a three-dimensional path plan leading to areas with optimal 5G communication strength, this study integrates 5G gravitational points into the traditional APF framework. These 5G gravitational points exert gravitational forces on UAV, directing it toward regions with superior 5G communication capabilities. It is crucial to note that once a sub-gravity point has fulfilled its guiding role for the UAV, its gravitational force must be reset to zero to prevent hindrance to the UAV's navigation towards the target destination. The gravitational force, denoted as $F_{5G}(X)$, exerted by a 5G sub-gravity point on the UAV as follows:

$$F_{5G}(X)$$
$$= \begin{cases} -K_{5G} \cdot \rho(X, X_{5G}), & else \\ 0, & \rho(X, X_{5G}) > \rho(X, X_d) \\ & \&\& \frac{d\rho(X, X_{5G})}{dX} > 0 \end{cases} \quad (27)$$

where $\&\&$ means that the condition $\rho(X, X_{5G}) > \rho(X, X_d)$ and the condition $\frac{d\rho(X, X_{5G})}{dX} > 0$ are established at the same time, $X_{5G} = (x_{5G}, y_{5G}, z_{5G})$ is the coordinate of the sub-gravity point, $\rho(X, X_{5G})$ is the Euclidean distance from the UAV to the sub-gravity point, K_{5G} is the potential field constant of the sub-gravity point.

The selection of coordinates for 5G gravitational points is contingent upon several factors, including the distribution of 5G communication intensity, the starting and target points of the path, as well as the distribution of obstacles and
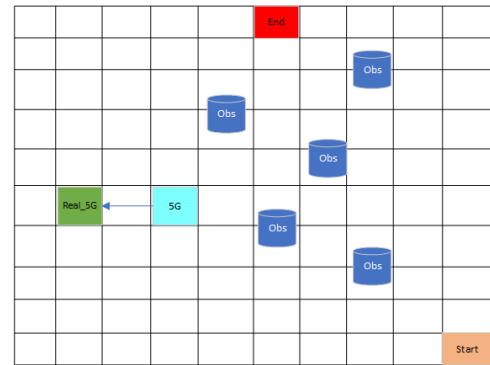
other variables. When choosing 5G gravitational points, it's advisable to adhere to the following four conditions:

1. The coordinate of the 5G sub-gravity point should not deviate entirely from the target point. It should be capable of guiding the path in certain sections, while being set to zero in areas where it might hinder progress.

2. When multiple 5G sub-gravity points are present, they should be distributed reasonably and evenly along the path. Otherwise, the guiding influence of each gravity point on the UAV may diminish due to mutual interference.

3. The coordinate of the 5G gravitational point must maintain a certain distance from obstacles. Failure to do so can weaken the guiding effect of the 5G gravitational point on the drone, owing to the spatial relationship between the obstacle, the 5G gravitational point, and the drone.

4. As the gravity of the 5G sub-gravity point is proportional to $\rho(X, X_{5G})$, when delineating the regional distribution of 5G communication intensity, it is advisable for the coordinate of the 5G sub-gravity point to be situated in proximity to areas with high 5G communication intensity. This ensures that the sub-gravity point exerts a stronger attractive force, effectively guiding the drone towards areas with optimal 5G communication intensity. The schematic diagram for selecting 5G gravitational points as shown in Fig.3.

D. THE SCHEMATIC DIAGRAM FOR SELECTING 5G GRAVITATIONAL POINTS

After the introduction of 5G gravitational points, the force dynamics of UAV in three-dimensional space become more intricate. The function representing the total force acting on the UAV in (5) requires modification. The adjusted total force function as follows:

$$F(X) = F_{att}(X) + \sum_{i=1}^{m} F_{rep}(X) + \sum_{j=1}^{l} F_{5G}(X) \quad (28)$$

where the definition of $F_{att}(X)$ is provided in (2), the definition of $F_{rep}(X)$ is provided in (24). The definition of $F_{5G}(X)$ is provided in (27). $\sum_{i=1}^{m} F_{rep}(X)$ signifies that the UAV is within the influence range of m obstacles.

$\sum_{j=1}^{l} F_{5G}(X)$ indicates that the UAV is influenced by l 5G gravitational points.

A new force, denoted as $F_o(X)$, is introduced to signify the UAV's potency, excluding the gravitational pull exerted by the target point. The expression for $F_o(X)$ as follows:

$$F_o(X) = \sum_{i=1}^{m} F_{rep}(X) + \sum_{j=1}^{l} F_{5G}(X) \qquad (29)$$

In scenarios where multiple forces act upon the UAV, it remains susceptible to being ensnared in a local minimum trap, characterized by the possibility of $F(X) = 0$.

To prevent the UAV from falling into the local minimum problem, it requires the addition of a new auxiliary force to aid its escape from such situations. In this study, a fuzzy control algorithm is employed to generate this auxiliary force. In the intricate three-dimensional space, especially after the incorporation of 5G gravitational points, the UAV's forces exhibit significant uncertainty. The fuzzy control algorithm proves effective in handling such uncertain information. In [22], a fuzzy control algorithm was proposed to generate an auxiliary force, enabling an Automated Guided Vehicle to evade local minima. However, this method was designed for application in two-dimensional space and does not account for the complexities of three-dimensional space.

In this study, the Mandani fuzzy algorithm is utilized to determine the magnitude of the additional auxiliary force, denoted as $F_f(X)$. The core concept of the Mandani fuzzy algorithm revolves around constructing a fuzzy control system. In this system, both input and output are obscured or blurred. Precise input and output values are mapped to discrete fuzzy variable subsets through membership functions, thus replacing these exact values with fuzzy linguistic terms. These fuzzy variable subsets typically include: negative big (NB), negative small (NS), zero (ZO), positive small (PS), and positive big (PB). A numerical scale $\{-2, -1, 0, 1, 2\}$ is commonly employed to correspond to these five fuzzy variable subsets. A fuzzy control system delineates the relationship between fuzzy input variables and fuzzy output variables by designing a rule base. Following the determination of fuzzy variable subsets and establishment of the rule base, the fuzzy variable for the output value can be derived through fuzzy reasoning based on the rule base, after obtaining the fuzzy variable for the accurate input value through membership functions. Subsequently, the fuzzy variable for the output value is converted into a precise value through defuzzification.

In this study, a dual-input and single-output fuzzy control system is devised to dynamically adjust the magnitude of the auxiliary force, thereby preventing the UAV from entering local minimum points. The system takes two inputs: $|F_d(X)|$ and θ_d, θ_d is the angle between $F_{att}(X)$ and $F_o(X)$. $\theta_d \in [-\pi, \pi]$. The output of the system is $|F_f(X)|$, with $|F_f(X)| \in [-1, 1]$. $F_d(X)$ is defined as:

$$|F_d(X)| = \frac{|F_{att}(X) - F_o(X)|}{|F_{att}(X)| + |F_o(X)|} \qquad (30)$$
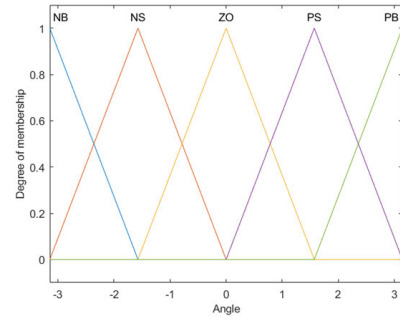

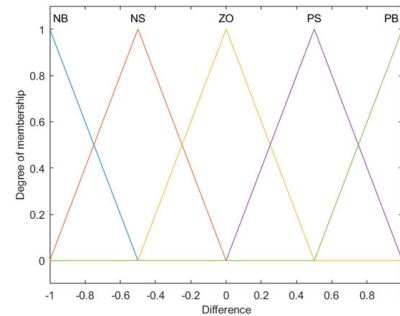FIGURE 4. Membership function diagram (a).
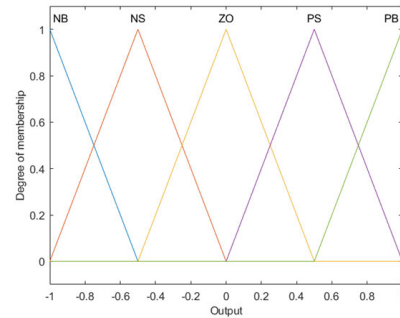

FIGURE 5. Membership function diagram (b).

FIGURE 6. Membership function diagram (c).

TABLE 1. Fuzzy rule base.

Difference	Angle				
	-2(NB)	-1(NS)	0(ZO)	1(PS)	2(PB)
-2(NB)	-2	-1	-1	0	1
-2(NS)	-2	-1	0	0	1
0(ZO)	-1	-1	0	1	1
1(PS)	-1	0	0	1	1
2(PB)	-1	0	1	1	2

The input and output of the fuzzy control system are triangular membership functions, as shown in Fig.4, Fig.5, and Fig.6.

In Fig.4, Fig.5, and Fig.6, Angle represents θ_d, Difference represents $|F_d(X)|$, and Output represents $|F_f(X)|$.

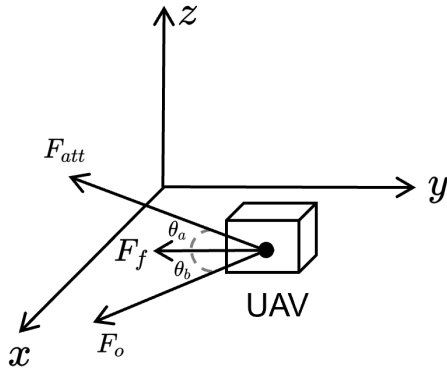The fuzzy rule base as shown in Table.1.

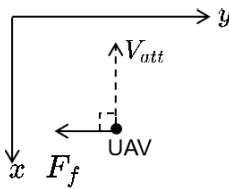**FIGURE 7.** The direction of auxiliary force.

FIGURE 8. The direction of $F_f(X)$ in the case of $F_{att}(X)$ and $F_o(X)$ reverse.

The fuzzy variable of the output value, derived through fuzzy reasoning, is defuzzified using the centroid method [23] to obtain the precise output value.

The direction of $F_f(X)$ is the direction of the angular bisection vector of $F_{att}(X)$ and $F_o(X)$, which as shown in Fig.7.

In Fig.7, θ_a is the angle between $F_{att}(X)$ and $F_f(X)$, θ_b is the angle between $F_o(X)$ and $F_f(X)$, and $\theta_a = \theta_b$.

When $F_{att}(X)$ is completely opposite to $F_o(X)$, $F_f(X)$ is parallel to the xOy plane. The projection vector of $F_{att}(X)$ on the xOy plane is set to be V_{att}, and the angle between $F_f(X)$ and V_{att} is 90 Â°, as shown in Fig.8

In conclusion, the force acting on the UAV as follows:

$$F(X) = F_{att}(X) + \sum_{i=1}^{m} F_{rep}(X) + \sum_{j=1}^{l} F_{5G}(X) + F_f(X)$$

(31)

V. EXPERIMENT

A. APF ALGORITHM CONSIDERING 5G COMMUNICATION FLOW

The flowchart of the artificial potential field algorithm considering 5G communication as shown in Fig.9.

B. EXPERIMENTAL ENVIRONMENT AND MODEL CONSTRUCTION

In this study, we constructed two maps measuring 400 × 400 meters in MATLAB R2023b. In the simulation, the carrier frequency is set to 50 GHz, the transmitting power is 10 W, the antenna height is 25 meters, and the system loss is 10 dB. The receiving power of the receiver is 10 W, with an antenna height of 1 meter and a system loss of 10 dB. The
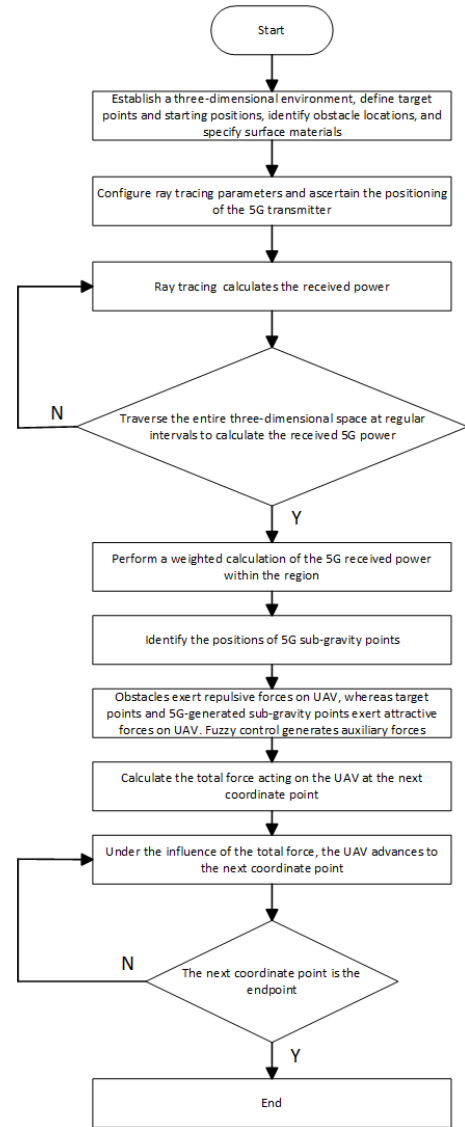

FIGURE 9. The algorithm flowchart of artificial potential field method considering 5G communication.

simulation accounts for 3 ray reflections and 1 diffraction, with a minimum receiving power of −140 dBm for the ray. Obstacle material is concrete. To facilitate the selection of 5G gravitational points, this study converts the unit of signal receiving power to Android Signal Strength(asu). The conversion relationship between ''asu'' and ''dBm'' as follows:

$$asu = dbm + 140$$

(32)

The gravitational potential field constant K_{att} is set to be 0.03, the repulsive potential field constant k_{rep} is set to be 0.8, n in the improved repulsive field function is set to be 2, the influence range of the obstacle repulsive force ρ_0 is set to be $2.5r_c$, r_c is the radius of the cylinder, and the sub-gravity point potential field constant K_{5G} is set to be 0.015.

To ascertain the 5G communication intensity across various regions within the three-dimensional environment, this
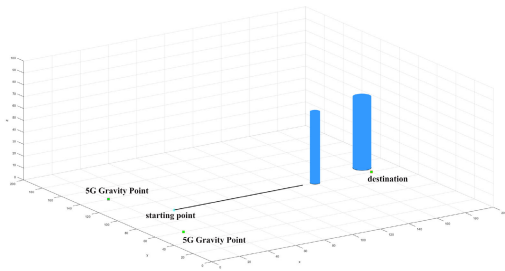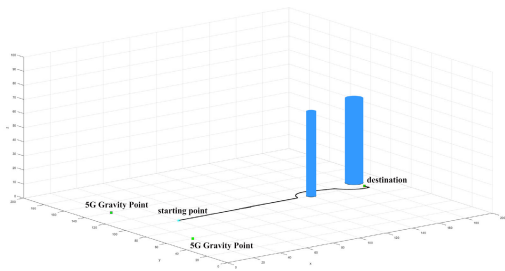
FIGURE 10. Improved APF.

FIGURE 12. Common scenario(a).

FIGURE 11. Improved APF.

FIGURE 13. Common scenario(b).

study adopts a fixed transmitter approach. It calculates the 5G communication intensity at discrete intervals across the entirety of the three-dimensional space and uniformly divides the region. Subsequently, the communication intensity at each point within each region is computed, weighted, and aggregated to derive a representative value for the 5G communication intensity of that region. This methodology is designed to facilitate the subsequent selection of 5G gravitational point coordinates.

C. COMPARISON OF IMPROVED ARTIFICIAL POTENTIAL FIELD METHOD

As shown in Fig.10, in the traditional APF, when the total force of the UAV is zero, it will fall into the local minimum problem and remain stationary, unable to reach the target point. As shown in Fig.11, the improved APF can avoid entering the local minimum point, and when the obstacle is near the target point, the UAV can also reach the target point normally.

D. COMPARISON OF IMPROVED ARTIFICIAL POTENTIAL FIELD METHOD

This study constructed three-dimensional maps with 26 and 27 obstacles in matlabR2023b. For the convenience of description, the map with 27 obstacles is named map A, and the map with 26 obstacles is named map B. In the simulation, the black path is obtained by APF without considering 5G communication, and the red path is obtained by APF considering 5G communication.

Table.2 presents the coordinates for the starting point, target point, base station, and three 5G gravitational points across the subsequent 8 simulation diagrams. Meanwhile,
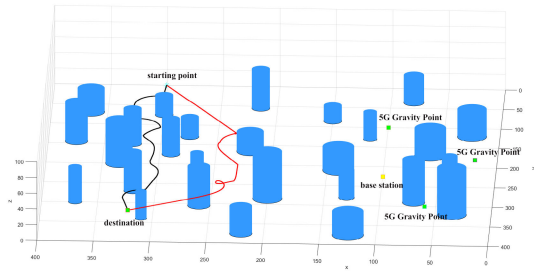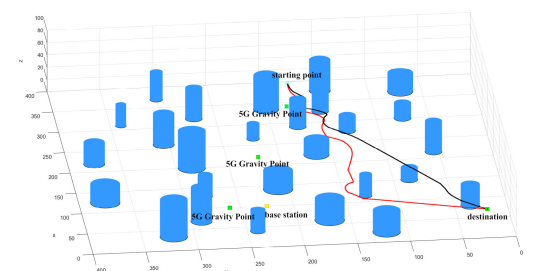
Table.3 outlines the step size and average 5G communication intensity along the path derived from the APF algorithm without accounting for 5G communication in these diagrams. Additionally, Table.3 further details the path's step size and average 5G communication intensity when considering 5G communication. Moreover, Table.3 provides insights into the path growth rate and the improvement rate of 5G communication intensity.

Each grid data within Table.4, Table.5, Table.6, and Table.7 represents the average 5G communication intensity within a 40 × 40 grid size on a 400 × 400 meters map. In these tables, the columns correspond to the x direction of the three-dimensional map, while the rows correspond to the y direction of the map. Specifically, Table.4 and Table.5 are computed using data from map A, whereas Table.6 and Table.7 are derived from map B. The selection of 5G gravitational points depicted in Fig.12 and 13 is based on the data presented in Table.4, while 14 and 15's selection of 5G gravitational points relies on Table.5. Similarly, 16 and 17's selection of 5G gravitational points corresponds to Table.6, and the selection of 5G gravitational points illustrated in 18 and 19 is informed by Table.7.

Fig.12 and Fig.13 are derived from Map A, with their base stations being identical. In Fig.12, the 5G communication intensity along the path, as obtained by APF with 5G communication taken into account, exhibits an increase of 16.6923%, while the path itself experiences a growth of 9.0909%. The amplification in 5G communication intensity surpasses the diminishing effect of path expansion. Conversely, in Fig.13, the 5G communication intensity along the path, obtained through APF considering 5G communication, registers a rise of 9.5508%, whereas the path grows by 10.5651%. Here,

TABLE 2. Simulation coordinate point.

	Starting point	Destination	Base station	5G Gravitational Point1	5G Gravitational Point2	5G Gravitational Point3
Fig.12	300,20,10	320,380,30	100,225,0	20,180,0	100,100,0	60,300,0
Fig.13	380,175,10	25,25,30	100,225,0	100,260,0	220,220,0	340,180,0
Fig.14	25,150,10	390,390,30	250,100,0	75,75,0	175,125,0	275,175,0
Fig.15	150,20,10	175,390,30	250,100,0	300,50,0	350,100,0	340,220,0
Fig.16	20,220,10	390,300,30	275,50,0	120,60,0	260,60,0	300,140,0
Fig.17	25,100,10	200,350,30	275,50,0	120,60,0	260,60,0	350,125,0
Fig.18	380,20,10	20,380,30	275,350,0	200,380,0	380,260,0	300,320,0
Fig.19	40,40,10	390,175,30	275,350,0	200,380,0	100,270,0	300,350,0

TABLE 3. Improve the comparison.

	original step length (m)	Improved step length (m)	original signal intensity (asu)	Improved signal intensity (asu)	Step increase	Increased strength
Fig.12	407	444	30.465	35.5503	9.09%	16.69%
Fig.13	407	450	37.8543	41.4697	10.57%	9.55%
Fig.14	469	488	33.7622	40.5907	4.05%	20.23%
Fig.15	384	487	40.6713	49.8222	26.82%	22.50%
Fig.16	400	477	35.5671	41.4382	19.25%	16.51%
Fig.17	325	398	35.4422	42.7041	22.46%	20.49%
Fig.18	548	571	22.7322	30.9799	4.20%	36.28%
Fig.19	421	479	16.4382	20.3979	13.78%	24.09%

TABLE 4. Map A, Distribution of 5G communication intensity at the base station location (100, 225, 0).

41.1359	37.2663	38.5205	38.4319	51.9487	54.4221	44.7868	57.2765	45.9874	34.5987
42.226	48.4967	48.9933	43.3456	63.9893	58.7306	60.4866	47.6721	48.772	46.5979
45.3273	51.5966	51.1985	51.9907	58.4454	64.2077	61.3521	55.8832	52.3727	50.7932
35.5664	37.8733	45.2687	50.072	55.5507	66.1309	58.6865	52.7714	48.7357	49.3868
39.9462	45.2375	49.2558	52.177	36.5723	47.0872	54.9353	53.5943	42.6143	36.1705
42.248	36.0548	48.628	40.1708	34.9428	40.3689	51.8601	57.2594	47.8684	44.9563
36.0334	46.3278	42.2466	35.0373	26.72	32.6224	49.1613	49.9948	33.2057	39.4153
44.4446	42.9583	35.6407	30.4413	37.2417	33.5359	47.8126	44.0564	31.1622	36.5842
40.4028	26.6416	30.8463	31.1121	31.2747	42.3735	45.5615	42.3482	33.5231	29.9374
31.4967	26.8535	28.0489	36.7299	26.4249	37.1815	44.7223	36.9461	37.3852	30.7651

TABLE 5. Map A, Distribution of 5G communication intensity at the base station location (250, 100, 0).

35.8192	38.1748	44.2534	44.8593	33.5291	42.1175	38.6046	41.7828	32.4221	32.8536
38.5046	42.3454	44.3344	41.3086	55.8286	46.2753	42.3237	35.5496	44.4578	37.7982
51.4824	46.1972	46.2036	49.8551	48.766	45.211	34.8852	38.5677	31.2973	25.8453
48.8552	51.3987	51.486	49.4915	50.4293	58.8093	43.0485	32.0507	29.8586	33.8014
38.2395	52.8342	55.4839	54.6802	52.0855	41.7022	28.8598	30.4676	24.6619	26.0193
51.4974	45.7467	60.4834	58.4055	46.3699	41.2065	42.998	61.8824	42.9563	44.026
54.2033	59.0974	64.7527	60.4344	55.5103	47.9501	48.1656	38.617	36.809	35.9654
53.498	56.51	60.3004	53.8804	51.7675	47.1863	47.7977	45.3506	38.2166	36.3416
51.7382	44.4684	54.6639	59.7247	37.9789	47.7118	32.9219	30.1979	38.6447	38.8781
45.372	40.9222	50.9348	59.8304	36.8353	42.1745	33.6773	31.333	30.1435	31.1468

the augmentation in 5G communication intensity is eclipsed by the adverse impact of path enlargement. This occurrence can be attributed to the proximity of the coordinates of the 5G sub-gravity point to regions characterized by high 5G communication intensity. The objective is to enhance the attractiveness of the sub-gravity point and effectively guide the drone towards areas with optimal 5G communication intensity. The selection of the 5G gravitational point's position in Fig.12 aligns more closely with this principle.

Fig.14 and Fig.15 are derived from Map A, sharing the same base stations. In Fig.14, the 5G communication intensity along the path, as computed by APF with 5G communication factored in, exhibits a notable increase of 20.2253%, while the path itself experiences a modest growth of 4.0512%. Here, the enhancement in 5G communication intensity outweighs the adverse impact of path expansion. Conversely, in Figure 15, the 5G communication intensity along the path, derived through APF considering 5G communication, shows a considerable rise of 22.4996%, whereas the path expands significantly by 26.8229%. In this scenario, the increase in 5G communication intensity is overshadowed by the substantial negative impact of path enlargement. This

TABLE 6. Map B, Distribution of 5G communication intensity at the base station location (275, 50, 0).

16.2586	28.8078	28.0539	37.1715	25.8651	37.6929	29.4538	41.2003	25.1359	24.6838
17.8647	26.4244	27.5317	46.0533	29.9929	30.4736	42.2971	33.0778	30.1152	23.8444
23.1238	48.4552	35.1641	36.7627	35.847	42.1007	47.0795	36.1378	46.9297	37.3031
31.217	28.7897	39.218	51.0715	43.5919	43.2173	40.8172	37.9406	27.0427	24.5777
40.4548	45.8917	47.1679	46.2039	49.3487	48.3792	31.9378	28.1263	29.7805	32.8956
53.4022	57.9436	55.626	57.0508	43.1368	41.5956	44.2177	44.6929	44.5281	41.3407
59.9081	67.4878	58.5444	54.3926	51.4246	49.0412	47.4638	44.7156	35.3339	36.9624
60.8441	62.8234	58.6021	49.5616	43.0407	33.6369	31.81	33.3403	50.4412	32.537
46.9013	59.9032	56.8331	57.866	43.019	49.7196	45.8282	41.0188	28.5519	22.3756
43.894	56.0592	47.1004	53.3223	46.5484	46.4515	47.0954	34.152	27.7641	27.1662

TABLE 7. Map B, Distribution of 5G communication intensity at the base station location (275, 350, 0).

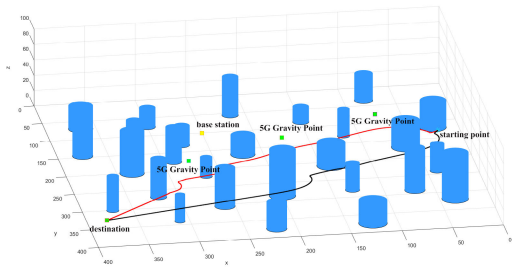|									
16.2586	28.8078	28.0539	37.1715	25.8651	37.6929	29.4538	41.2003	25.1359	24.6838
17.8647	26.4244	27.5317	46.0533	29.9929	30.4736	42.2971	33.0778	30.1152	23.8444
23.1238	48.4552	35.1641	36.7627	35.847	42.1007	47.0795	36.1378	46.9297	37.3031
31.217	28.7897	39.218	51.0715	43.5919	43.2173	40.8172	37.9406	27.0427	24.5777
40.4548	45.8917	47.1679	46.2039	49.3487	48.3792	31.9378	28.1263	29.7805	32.8956
53.4022	57.9436	55.626	57.0508	43.1368	41.5956	44.2177	44.6929	44.5281	41.3407
59.9081	67.4878	58.5444	54.3926	51.4246	49.0412	47.4638	44.7156	35.3339	36.9624
60.8441	62.8234	58.6021	49.5616	43.0407	33.6369	31.81	33.3403	50.4412	32.537
46.9013	59.9032	56.8331	57.866	43.019	49.7196	45.8282	41.0188	28.5519	22.3756
43.894	56.0592	47.1004	53.3223	46.5484	46.4515	47.0954	34.152	27.7641	27.1662

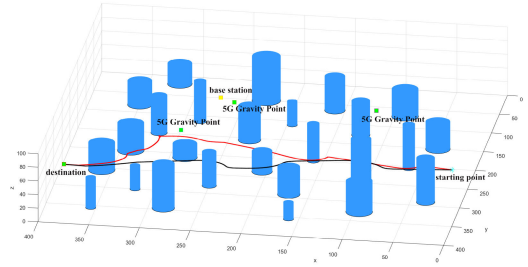

FIGURE 14. Common scenario(c).
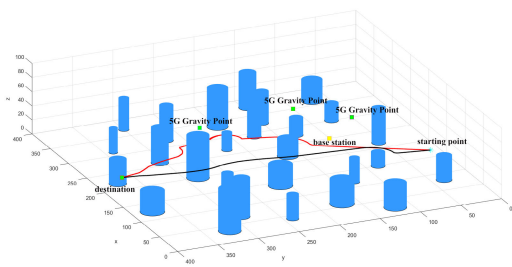

FIGURE 16. Common scenario(e).

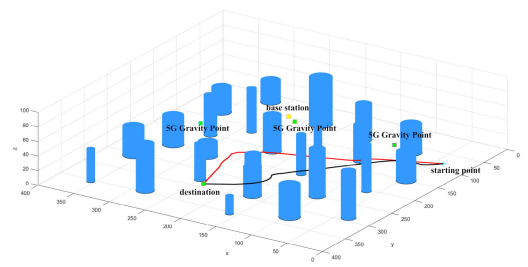**FIGURE 15.** Common scenario(d).

FIGURE 17. Common scenario(f).

phenomenon arises due to the presence of multiple 5G sub-gravity points. It is imperative that these points are reasonably and evenly distributed along the path. Failure to do so may result in the weakening of the guiding effect of each gravity point on the drone, as they could potentially interfere with each other. The distribution of 5G gravitational points in Fig.14 adheres more closely to this principle.

Fig.16 and Fig.17 are generated from Map B, with identical base stations. In Figure 16, the 5G communication intensity along the path, as determined by APF with 5G

communication considerations, demonstrates a growth of 16.5071%, while the path itself expands by 19.2500%. However, the increase in 5G communication intensity is surpassed by the negative impact of path growth. Similarly, in Fig.17, the 5G communication intensity along the path increases by 20.4894%, while the path grows by 22.4615%. Again, the gain in 5G communication intensity is overshadowed by the adverse effect of path expansion. This phenomenon can be attributed to the positioning of the 5G gravitational point relative to obstacles. It's crucial for the coordinates of the
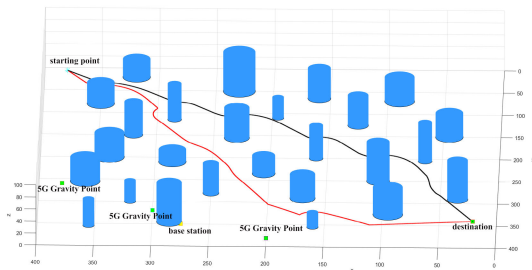
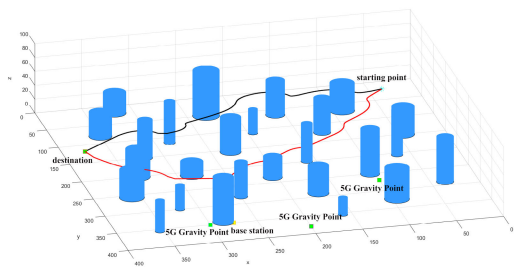**FIGURE 18.** Severe signal masking scenario(a).

FIGURE 19. Severe signal masking scenario(b).

5G gravitational point to maintain a certain distance from obstacles. Otherwise, due to the spatial relationship between the obstacle, the 5G gravitational point, and the UAV, the guidance provided by the 5G gravitational point to the UAV may be compromised. However, in Fig.16 and Fig.17, there is an abundance of obstacles around the starting point, which weakens the effectiveness of the 5G gravitational points in guiding the UAV.

Fig.18 and Fig.19, derived from Map B, share identical base stations. In Fig.18, the 5G communication intensity along the path, computed by APF with 5G communication considerations, exhibits a substantial increase of 36.2820%, while the path itself experiences a modest growth of 4.1971%. Here, the enhancement in 5G communication intensity outweighs the negative impact of path expansion. Similarly, in Fig.19, the 5G communication intensity along the path increases by 24.0884%, whereas the path expands by 13.7767%. In this case, the gain in 5G communication intensity significantly surpasses the adverse effect of path enlargement. This phenomenon arises due to the severe obstruction of transmitter signals by obstacles, resulting in significant variations in the 5G communication intensity across different regions of the map. The presence of 5G secondary gravity points plays a crucial role, leading to a more pronounced increase in the average 5G communication intensity calculated along the path obtained through APF considering 5G communication. This indicates that the algorithm proposed in this study exhibits superior adaptability and feasibility in scenarios with severe signal masking at the transmitter. Conversely, when map obstacles are evenly distributed, resulting in minimal differences in 5G communication intensity across regions, the proposed algorithm may exhibit limitations. In such scenarios, the

improvement in 5G communication intensity is typically less pronounced.

VI. CONCLUSION AND FUTURE WORK

In this study, addressing the common oversight in existing three-dimensional path planning schemes which fail to account for 5G communication intensity, an enhanced APF algorithm is proposed which is incorporating 5G sub-gravity points. Aiming at the local minimum traps inherent in traditional APF algorithm, a fuzzy control algorithm is proposed to enable UAVs to avoid the local minimum traps in advance.

Using MATLAB R2023b, simulations of the proposed algorithm are conducted and 8 sets of experimental data across two maps are obtained. The simulation results show that the average 5G communication intensity of the path increases by 20.7919%, while the average length of the path increases by 13.7769%. Notably, the enhancement in average 5G communication intensity along the path is more pronounced in scenarios with severe signal masking at the transmitter. Simulation results show the feasibility and adaptability of the proposed algorithm.

For future optimization endeavors, our focus will be on designing a more reasonable algorithm to select optimal 5G gravitational point coordinates based on available map and base station data. Additionally, utilizing a quadcopter UAV for experiments in real urban environment is planned. These experiments aim to validate the feasibility and efficacy of the algorithm in real-world scenarios, thus advancing our understanding and application of 5G-enabled UAV path planning in urban settings.

REFERENCES

[1] E. W. Dijkstra, "A note on two problems in connexion with graphs," in *Edsger Wybe Dijkstra: His Life, Work, and Legacy*. New York, NY, USA: ACM, 2022, pp. 287–290.

[2] L. De Filippis, G. Guglieri, and F. Quagliotti, "Path planning strategies for UAVS in 3D environments," *J. Intell. Robotic Syst.*, vol. 65, nos. 1–4, pp. 247–264, Jan. 2012.

[3] J. H. Holland, *Adaptation in Natural and Artificial Systems: An Introductory Analysis With Applications to Biology, Control, and Artificial Intelligence*. Cambridge, MA, USA: MIT Press, 1992.

[4] J. Kennedy and R. Eberhart, "Particle swarm optimization," in *Proc. Int. Conf. Neural Netw. (ICNN)*, Nov./Dec. 1995, pp. 1942–1948.

[5] M. Dorigo, V. Maniezzo, and A. Colorni, "Ant system: Optimization by a colony of cooperating agents," *IEEE Trans. Syst., Man, Cybern., B (Cybern.)*, vol. 26, no. 1, pp. 29–41, Feb. 1996.

[6] O. Khatib, "Real-time obstacle avoidance for manipulators and mobile robots," in *Proc. IEEE Int. Conf. Robot. Automat.*, Mar. 1985, pp. 500–505.

[7] M. G. Park and M. C. Lee, "A new technique to escape local minimum in artificial potential field based path planning," *KSME Int. J.*, vol. 17, no. 12, pp. 1876–1885, Dec. 2003.

[8] M. G. Park, J. H. Jeon, and M. C. Lee, "Obstacle avoidance for mobile robots using artificial potential field approach with simulated annealing," in *Proc. IEEE Int. Symp. Ind. Electron. (ISIE)*, Jun. 2001, pp. 1530–1535.

[9] Y. Zhu, T. Zhang, and J. Song, "An improved wall following method for escaping from local minimum in artificial potential field based path planning," in *Proc. 48th IEEE Conf. Decis. Control (CDC) Held Jointly 28th Chin. Control Conf.*, Dec. 2009, pp. 6017–6022.

[10] X.-Y. Zou and J. Zhu, "Virtual local target method for avoiding local minimum in potential field based robot navigation," *J. Zhejiang Univ.-Sci. A*, vol. 4, no. 3, pp. 264–269, May 2003.

[11] M. Peter, K. Haneda, S. Nguyen, A. Karttunen, and J. Järveläinen, "Measurement results and final mmMAGIC channel models," *Deliverable D2*, vol. 2, no. 12, 2017.

[12] D. Riviello, R. Tuninato, E. Zimaglia, R. Fantini, and R. Garello, "Implementation of deep-learning-based CSI feedback reporting on 5G NR-compliant link-level simulator," *Sensors*, vol. 23, no. 2, p. 910, Jan. 2023.

[13] A. Maltsev, *Channel Models for 60 GHz WLAN Systems*, IEEE Standard 802.1109/0334r8, 2010.

[14] V. Nurmela, A. Karttunen, A. Roivainen, L. Raschkowski, V. Hovinen, Y. E. B. Juha, N. Omaki, K. Kusume, A. Hekkala, and R. Weiler, "Deliverable D1.4 METIS channel models," in *Proc. Mobile Wireless Commun. Enablers Inf. Soc. (METIS)*, vol. 1, 2015, p. 1.

[15] A. Maltsev, A. Pudeyev, A. Lomayev, and I. Bolotin, *Channel Models for IEEE 802.11 AY*, document 802.11-15/1150r9," IEEE, New York, NY, USA, 2016.

[16] Z. Yun and M. F. Iskander, "Ray tracing for radio propagation modeling: Principles and applications," *IEEE Access*, vol. 3, pp. 1089–1100, 2015.

[17] L. H. Wang, "Research on ray tracing simulation and modeling of millimeter-wave mobile channels," Ph.D. dissertation, Dept. Commun. Inf. Syst., Univ. Beijing, Beijing, China, 2022.

[18] S. L. McGregor and J. Pleasants, "Shedding light on boundaries: Re-sequencing Snell's law instruction to first build conceptual understanding," *Phys. Educ.*, vol. 57, no. 5, Sep. 2022, Art. no. 055018.

[19] P. D. Holm, "A new heuristic UTD diffraction coefficient for nonperfectly conducting wedges," *IEEE Trans. Antennas Propag.*, vol. 48, no. 8, pp. 1211–1219, Aug. 2000.

[20] S. S. Ge and Y. J. Cui, "New potential functions for mobile robot path planning," *IEEE Trans. Robot. Automat.*, vol. 16, no. 5, pp. 615–620, Oct. 2000.

[21] Y. C. Guo, X. X. Liu, W. G. Zhang, and Y. Yang, "3D path planning method for UAV based on improved artificial potential field," *J. Northwestern Polytech. Univ.*, vol. 38, no. 5, pp. 977–986, 2020.

[22] P. Zhou, D. Wu, Y. He, and Y. Pan, "Improved path planning algorithm based on fuzzy control combining A* artificial potential field method," in *Proc. 34th Chin. Control Decis. Conf. (CCDC)*, Aug. 2022, pp. 4640–4645.

[23] N. Pfluger, J. Yen, and R. Langari, "A defuzzification strategy for a fuzzy logic controller employing prohibitive information in command formulation," in *Proc. IEEE Int. Conf. Fuzzy Syst.*, Mar. 1992, pp. 717–723.

HAOXIAN CHEN was born in Foshan, Guangdong, in 2003. He is currently pursuing the B.S. degree in electronic information engineering with South China Agricultural University. His research interests include path planning and digital image processing.

ZHAOYONG MA was born in Shantou, Guangdong, in 2002. He is currently pursuing the B.S. degree in electronic information engineering with South China Agricultural University. His research interests include path planning and SLAM.

ZICHEN JIN was born in Shouzhou, Shanxi, in 2003. She is currently pursuing the B.S. degree in electronic information engineering with South China Agricultural University. Her research interests include quadcopter drone.

YESHUANG TANG was born in Chongqing, in 2002. He is currently pursuing the B.S. degree in electronic information engineering with South China Agricultural University. His research interests include fifth generation mobile communication technology and quadcopter drone.

HUILI YIN received the M.S. degree from the School of Automation Science and Engineering, South China University of Technology, in 2003. She taught with the College of Electronic Engineering (College of Artificial Intelligence), South China Agricultural University, in 2003. She has been teaching for more than 20 years and is currently a Senior Teacher. She has authored more than ten technical papers in journals and conferences. Her current research interests include agricultural information technology and agricultural automation.

• • •